Thin–Walled Structures 224 (2026) 114686

Contents lists available at ScienceDirect

Thin-Walled Structures

journal homepage: www.elsevier.com/locate/tws

Behaviour and design of 6082-T6 aluminium lap joints at ambient temperature and post-fire

Michaela Gkantou [a,*], Manuela Cabrera [b], Marina Bock [c], Marios Theofanous [d]

[a] School of Engineering and Built Environment, Liverpool John Mores University, UK
[b] James Watt School of Engineering, University of Glasgow, UK
[c] Department of Civil Engineering, Aston University, UK
[d] Department of Civil Engineering, School of Engineering, University of Birmingham, UK

ARTICLE INFO

Keywords:
Aluminium alloys
Post-fire
Joints
Bearing
Net section
Fracture

ABSTRACT

Structural aluminium alloys are commonly heat-treated to enhance their strength for load-bearing applications, but exposure to fire can degrade or completely eliminate these benefits. Even if a component withstands the fire, it may no longer meet design load requirements, making post-fire performance assessment essential. This study presents 16 material coupons tests and 12 experimental tests on 6082-T6 aluminium lap joints exposed to elevated temperatures (200 °C, 300 °C, and 400 °C) prior to testing. Three joint configurations with varying bolt spacing were investigated, resulting in different failure modes: net section fracture, end bearing, and mixed failure. One unheated specimen per configuration served as a benchmark sample. Additionally, tensile tests on flat and flat grooved coupons were conducted to characterise the stress-strain and fracture behaviour after thermal exposure. The findings of the lap joint tests include load-displacement behaviour, as well as evaluations of failure loads and failure modes, and are reported in detail. Subsequently, numerical models were developed and validated against the experimental results. A parametric study was also carried out to investigate the influence of the bolt hole end and edge distance on the joint performance. The experimental and numerical results were used to evaluate the accuracy of existing design standards for predicting the resistance of aluminium alloy connections, including AS/NZS 1664.1, EN 1999-1-1 (Eurocode 9), and the provisions available in the literature. Based on the experimental and numerical data, a modified design equation for the bearing resistance factor is proposed to improve the prediction accuracy, and enable post-fire design that accounts for temperature-induced degradation.

1. Introduction

Aluminium alloys have attracted considerable interest in structural engineering research over the past two decades, primarily due to their advantageous combination of high strength-to-weight ratio, corrosion resistance, and recyclability [1–6]. These properties make them ideal candidates for applications in aerospace, transportation, marine, and increasingly, in building and civil infrastructure systems. There are eight aluminium series each characterised by its principal alloy element with the 6xxx and 7xxx series aluminium alloys being suitable for structural applications. Among them, the 6082-T6 aluminium alloy stands out due to its high strength, good weldability and good corrosion resistance. The T6 temper process, involving solution heat treatment followed by artificial aging, significantly enhances the mechanical performance of the alloy, making it suitable for load-bearing components.

This study investigates the structural performance of aluminium alloy lap joints fabricated from 6082-T6. Lap joints, formed by overlapping metal plates and securing them with bolts, are among the most prevalent types of mechanical joints used in civil engineering and industrial structures. Their ease of assembly makes them essential components in bolted connections for aluminium frameworks. Existing studies on aluminium alloy connections and joints have reported that current code-based design approaches generally lead to conservative strength predictions, highlighting the need for further research [1]. This conservatism arises because many of the formulations are adapted from steel-based equations with simplified bilinear material models, do not adequately capturing aluminium's nonlinear stress–strain behaviour, and are often based on limited experimental and numerical data.

* Corresponding author.
E-mail address: m.gkantou@ljmu.ac.uk (M. Gkantou).

https://doi.org/10.1016/j.tws.2026.114686
Received 21 November 2025; Received in revised form 14 February 2026; Accepted 15 February 2026
Available online 16 February 2026

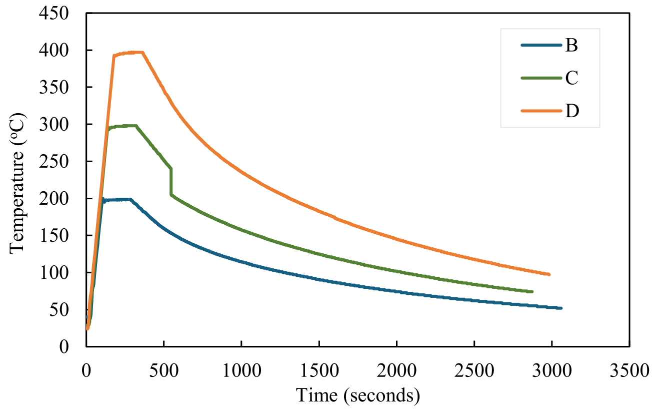

Fig. 1. Heating protocol.

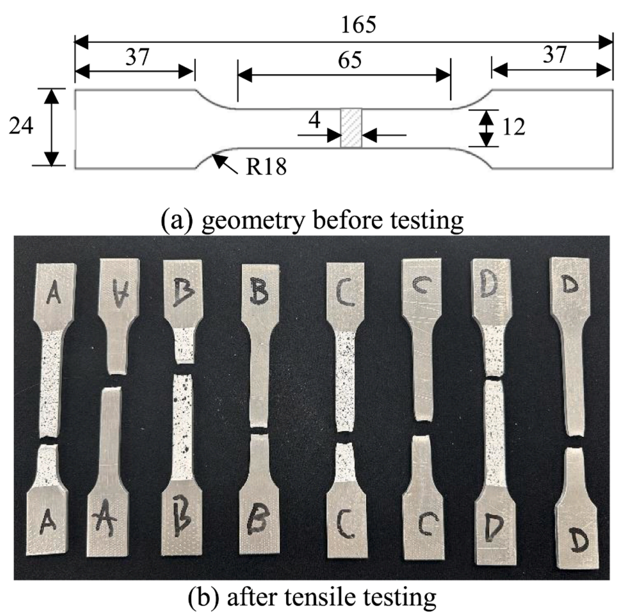

Fig. 2. Tensile flat coupon tests.

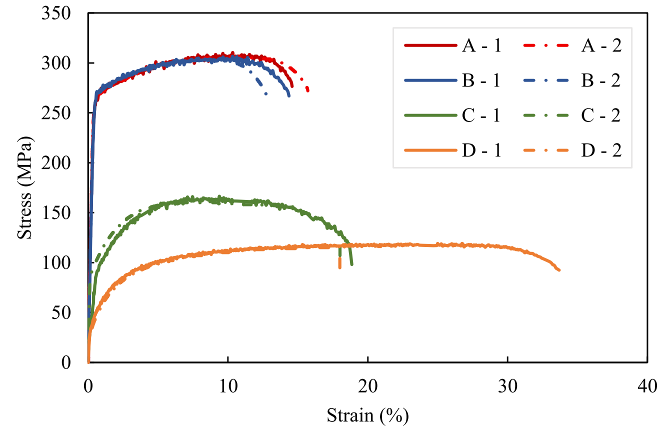

Fig. 3. Stress-strain curves from flat coupon tests.

Although recent studies have examined various aluminium alloy connection configurations under ambient temperature conditions [7,8], research specifically focused on the behaviour of lap joints remains limited.

A key limitation of aluminium alloys, including 6082-T6, is their mechanical degradation under elevated temperature exposure [9–13]. Wang et al. [14] reviewed recent research on the mechanical properties and structural fire behaviour of aluminium alloy structures during and after fire, identifying key areas for future investigation to support wider structural application, including the need for focused studies on post-fire performance of alloy connections to enable more reliable and accurate design methods. On this direction, several studies have examined the material properties degradation [6,7,15] or the performance of beams or columns at elevated temperatures [11–13,16]; however, limited research exists on how thermal exposure affects the ultimate performance and failure mode of bolted connections - a critical component in structural assemblies. Maljaars and De Matteis [17] conducted both experimental and numerical studies on T-stub bolted connections made from 6060-T6 aluminium alloy, focusing on their structural behaviour and strength at elevated temperatures. Liu et al. [18] investigated single shear bolted connections using 6061-T6 aluminium alloy. Wang et al. [19] performed shear connection tests on 7A04-T6 aluminium alloy to assess the in-fire and post-fire capacities of single shear bolted connections, with particular focus on end distance effects and the validity of existing design codes. Additionally, Guo et al. [20] studied the fire resistance of gusset joints fabricated from 6061-T6 and 6063-T5 aluminium alloys and proposed theoretical equations for predicting their strength and stiffness. At another study [21], Guo et al. examined the high-temperature flexural behaviour of aluminium alloy beam–column joints with bolted double steel clamp plates, quantifying temperature-dependent failure modes, stiffness degradation, and moment capacity reduction.

Despite extensive research on aluminium alloy connections, the high-temperature and post-fire behaviour of bolted joints-particularly those made from the widely used 6082-T6 alloy-remains insufficiently understood. This study addresses this gap through combined experimental and numerical investigation of the residual performance of bolted aluminium joints after exposure to elevated temperatures. At post-fire conditions, bolted aluminium alloy joints exhibit altered ductility and, in some cases, different governing failure modes due to irreversible thermal degradation and changes in load redistribution, rather than simply reduced strength values. Consequently, the post-fire structural behaviour cannot always be represented as a scaled ambient-temperature response, highlighting the relevance of the present research. By integrating mechanical testing, numerical modelling, and code assessment, the study provides critical insight into the adequacy of current aluminium design provisions, including recent updates to EN 1999-1-1 [22], and supports the development of safer and more resilient aluminium structures for post-fire applications, such as those encountered in fire events or industrial high-heat environments. As the construction industry moves toward lightweight and sustainable solutions, studies such as the present one, underpin the reliable integration of aluminium alloys in modern structural systems and promote reuse and recyclability.

The experimental programme reported herein includes results from twelve bolted lap joint specimens, eight flat coupon specimens, and eight flat grooved coupons tests. The test matrix is designed to explore both strength and ductility degradation due to thermal preconditioning at various temperature levels. Section 2 presents the heating protocol and material testing. Section 3 describes the lap joint testing procedures and results. Section 4 includes a detailed numerical model validation and a parametric investigation using finite element analysis. In Section 5, the test results are evaluated against the design predictions of current

Table 1
Summary of measured material properties.

Specimen	T (°C)	E_0 (MPa)	f_0 (MPa)	f_u (MPa)	ε_u (%)	ε_f (%)	n	m	Reduction factor 6082-T6		Reduction factor 6063-T5 [23]	
									f_0	f_u	f_0	f_u
A	20	72004	265	306	11.3	15.7	30.0	2.5	-	-	-	-
B	200	70371	263	303	9.3	12.8	30.0	3.0	0.99	0.99	~1.0	~1.0
C	300	67363	93	160	7.8	18.0	9.0	4.0	0.34	0.52	~0.49	~0.61
D	400	68000	43	123	27.0	33.6	3.0	14.0	0.16	0.40	~0.13	~0.38

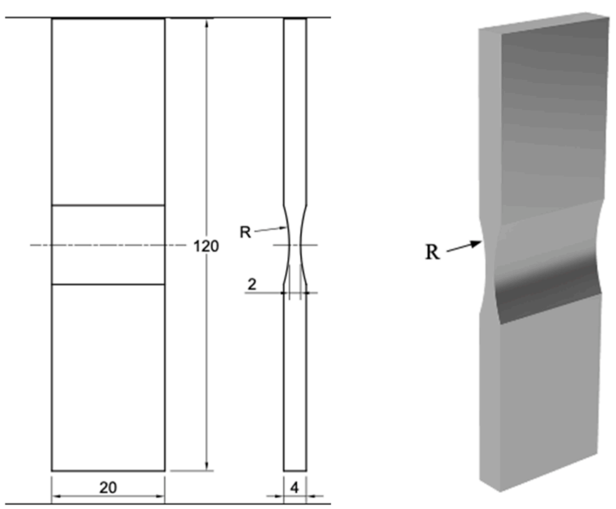

(a) dimensions in mm (b) 3D sketch.

Fig. 4. Flat-grooved coupon geometry.

structural standards, whilst Section 6 concludes with key findings.

2. Material testing

2.1. Heating protocol

Both lap joint specimens and tensile coupons were initially exposed to elevated temperatures to simulate post-fire conditions and assess residual performance. Three elevated-temperature exposure protocols were applied, involving heating to 200 °C, 300 °C, and 400 °C, followed by natural cooling as described in [23]. The specimens and material coupons were gradually heated from ambient temperature at a controlled rate of 15 °C per minute. The furnace used for this process featured multiple uniformly spaced heating elements to ensure consistent thermal conditions. Upon reaching the target temperature, a holding period of 30 min was implemented to promote uniform heat distribution throughout each sample. Following the dwell period, the furnace was switched off, and all specimens were allowed to cool naturally to room temperature inside the chamber. Tests were also conducted on specimens not subjected to elevated temperatures to serve as a benchmark. Henceforth in the discussion and in the figures, room-temperature specimens are labelled as Group A. Those subjected to elevated temperatures are categorised as follows: Group B for samples heated to 200 °C, Group C for 300 °C, and Group D for 400 °C, as shown in Fig. 1. The abrupt temperature drop in curve C likely resulted from a furnace preset limit and can be considered acceptable, as the target thermal response had already been achieved.

2.2. Material flat coupon tests

All tested specimens were made of aluminium alloy 6082-T6 according to [22]. The aluminium material used in this study was sourced from Simmal Ltd [24]. Tensile tests were performed on standard flat coupons extracted from the same plate used to manufacture the samples described in Section 3. The geometry of these coupons is illustrated in Fig. 2 (a). All coupons had a thickness of 4 mm, consistent with that of the lap joint specimens. The tests were carried out in accordance with the procedure outlined in EN ISO 6892-1 [25], using a 50 kN hydraulic tensile testing machine, and the tensile load was applied under displacement control at a rate of 0.2 mm/min. The failed specimens are shown in Fig. 2 (b). The obtained stress-strain behaviour of all eight coupon tests is presented in Fig. 3. To verify the consistency and repeatability of the results, duplicate tests were carried out for each specimen. The average material properties obtained from the dog-bone coupon tests are reported in Table 1, where E_0 is the Young's modulus, f_0 is the 0.2 % proof stress, f_u is the ultimate stress, ε_u is the strain at

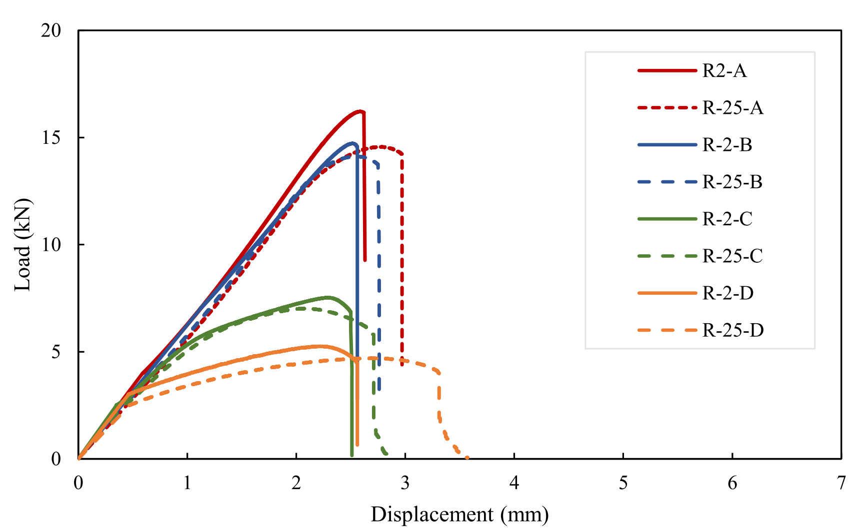

Fig. 5. Stress-strain curves from flat grooved coupon tests.

(a) R=2 mm (b) R=25 mm

Fig. 6. Flat grooved coupons after tensile testing.

Table 2
Lap-joint sample list, dimensions and bolt arrangement.

Specimen	Number of bolts	*T* (°C)	*d* (mm)	d_0 (mm)	e_1 (mm)	e_2 (mm)	*h* (mm)
1A	4	20	12	13	40	20	260
1B	4	200	12	13	40	20	260
1C	4	300	12	13	40	20	260
1D	4	400	12	13	40	20	260
2A	3	20	12	13	17	20	187
2B	3	200	12	13	17	20	187
2C	3	300	12	13	17	20	187
2D	3	400	12	13	17	20	187
3A	3	20	12	13	30	20	200
3B	3	200	12	13	30	20	200
3C	3	300	12	13	30	20	200
3D	3	400	12	13	30	20	200

ultimate stress, ε_f is the strain at fracture, and n and m are the two parameters for the Ramberg-Osgood model [26], fitted based on the experimental data. The mechanical properties summarised in Table 1 are used for finite element modelling (Section 4), while only the ultimate strength (f_u) is required for the code-based strength predictions (Section 5).

For coupons exposed to moderate temperatures (200 °C), the material exhibits only a slight reduction in strength, retaining most of its original properties. However, as the exposure temperature increases, both the 0.2 % proof stress (f_o) and ultimate tensile strength (f_u) decline significantly. Specifically, f_o drops from 265 MPa at 20 °C to 43 MPa at 400 °C, while f_u decreases from 306 MPa to 123 MPa over the same range, indicating a substantial loss in mechanical strength. Table 1 also shows the reduction factors compared to room temperature material properties, indicating a 0.16 reduction in proof strength and a 0.40 reduction in ultimate strength at 400 °C. Similar values have been reported by Sun et al. for another 6xxx aluminium alloy, with reduction factors of 0.13 for proof strength and of 0.38 for ultimate strength, after exposure at 401 °C [23]. On the contrary, both the ultimate strain and fracture strain increase significantly at 400 °C. This suggests that although the material weakens at higher temperatures, it gains greater ductility and post-yield deformation capacity. Lastly, the Young's modulus remains relatively stable across the tested temperature range.

2.3. Material flat grooved coupon tests

To develop a material fracture model, tests on material coupons subjected to different levels of stress triaxiality were also carried out [27, 28]. Two flat-grooved specimens for each examined temperature state (A, B, C, D) featuring a circumferential notch were tested. The notches were introduced to the specimens using a controlled machining process. The notch dimensions (depth, width, and radius) were defined in advance and verified using calibrated measurement tools after fabrication to minimise variability. The thickness of all coupons was 4 mm, consistent with the thickness used for all specimens, whilst at the notch location the minimum thickness was 1.95 mm. Two notch radii R equal to 2 mm and 25 mm were considered, as shown in Fig. 4, to capture the fracture characteristics of the material over a range of stress triaxiality levels η. The specimens were labelled according to the groove radius R in

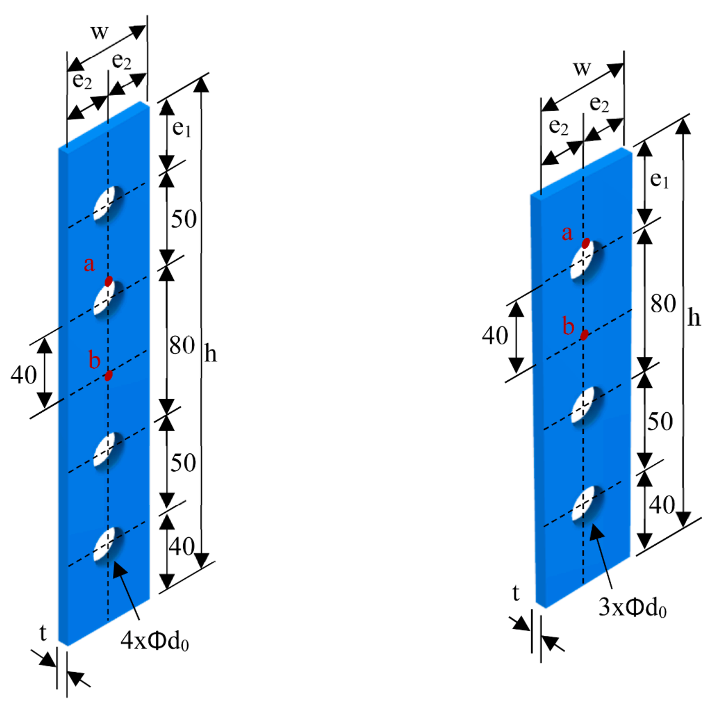

(a) Specimens Group 1 (b) Specimens Groups 2 and 3

Fig. 7. Lap joints geometry.

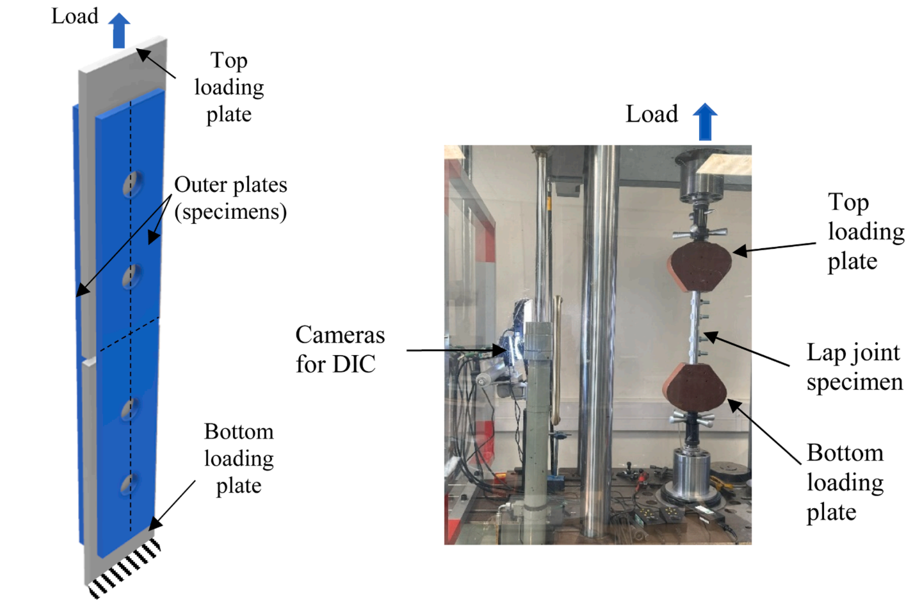

(a) Test arrangement (b) Photo of experimental set-up

Fig. 8. Experimental set-up.

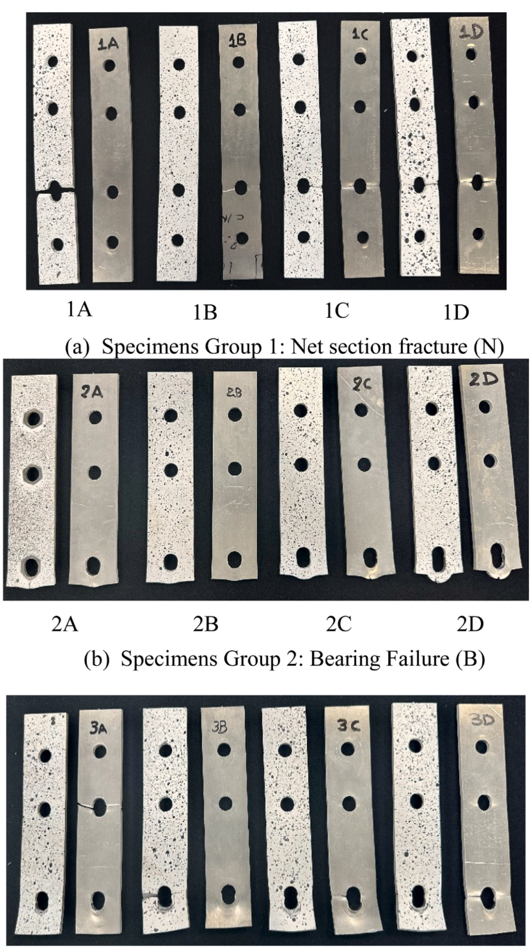

1A 1B 1C 1D

(a) Specimens Group 1: Net section fracture (N)

2A 2B 2C 2D

(b) Specimens Group 2: Bearing Failure (B)

3A 3B 3C 3D

(c) Specimens Group 3: Bearing Failure (B) + Net section fracture (N)

Fig. 9. Experimentally observed failure modes.

millimetres as R2 and R25. The obtained load-displacement curves and the corresponding failed specimens are presented in Fig. 5 and Fig. 6, respectively, and are aligned with those presented in [30].

3. Lap joint tests

3.1. Test set-up

A total of twelve tests were conducted on aluminium lap joints made from Grade 6082-T6, using the dimensions and bolt hole configuration shown in Fig. 7 and Table 2. Specimens of Group 1, designed to fail in pure net section fracture, featured four bolts (Fig. 7 (a)), whereas Specimens of Groups 2 and 3, designed to fail in pure bearing and combined bearing and net section fracture respectively, incorporated three bolts each but also differed in overall plate geometry and bolt spacing (Fig. 7 (b)). The experimental set-up, shown in Fig. 8 consisted of double-shear lap joints connecting the two (top and bottom) steel loading plates, which were clamped within the testing machine grips. The end and edge distances (e_1, e_2) and hole-to-hole spacings were deliberately varied to promote different failure mechanisms. All aluminium plates were fabricated from Grade 6082-T6 with a nominal thickness (t) of 4 mm, a width (w) of 40 mm, whilst the bolt hole diameter (d_o) was 13 mm. Key geometric parameters for each configuration are provided in Table 2.

The loading plates were machined from S355 structural steel, each with a thickness of 10 mm, and were designed to remain elastic throughout testing. The same pair of loading plates was reused for all tests. M12 Grade 8.8 bolts were employed, featuring an unthreaded shank length of 18 mm -comprising two 4 mm-thick aluminium plates and a 10 mm-thick steel plate- to ensure that no threads were present in the shear plane. Dimensional checks confirmed that the fabricated specimens closely matched the nominal design values; therefore, nominal dimensions were adopted for all analysis. All tests were conducted using a Mayes universal testing machine with a 500 kN load capacity. Displacement-controlled loading was applied at a constant rate of 0.5 mm/min until failure. Strain and deformation fields were captured using a Dantec Dynamics Digital Image Correlation (DIC) system. Two tracking points, labelled a and b, [29] were placed around the bolt holes (see Fig. 7 (a) and 7 (b)) to monitor deformation during testing and enable relevant load-displacement curves to be extracted.

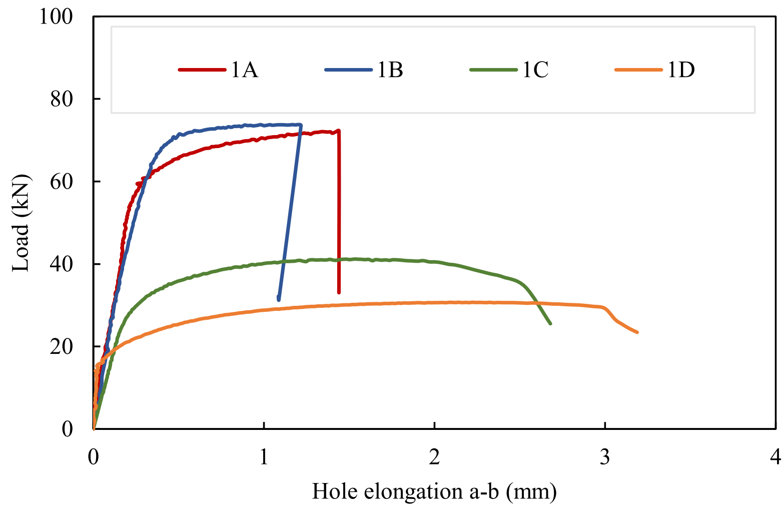

(a) Specimens Group 1

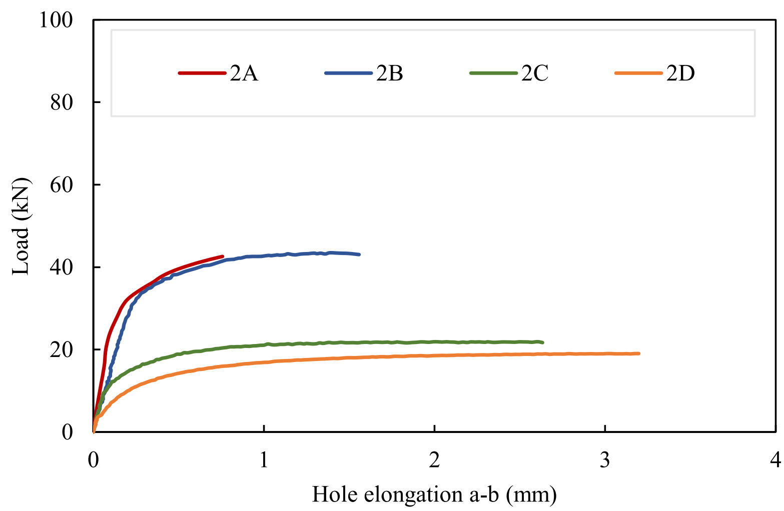

(b) Specimens Group 2

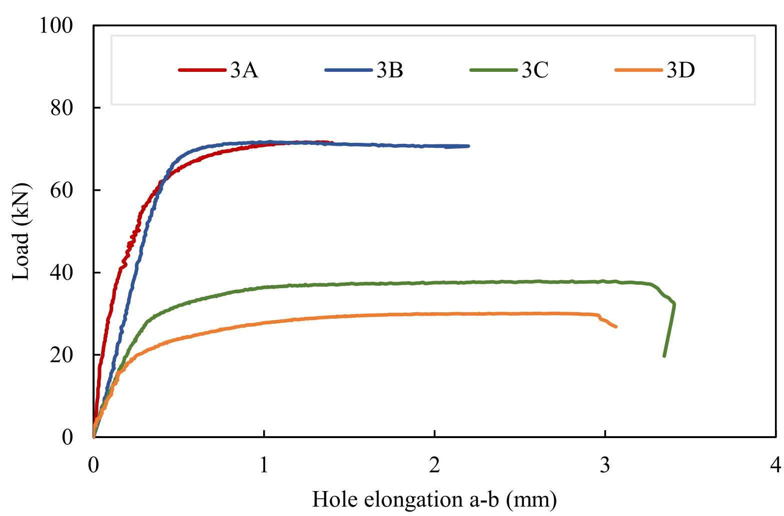

(c) Specimens Group 3

Fig. 10. Experimental load-displacement curves.

Table 3
Lap joint experimental results.

Specimen	T (°C)	f_u (MPa)	d_0 (mm)	α_b	$F_{u,test}$ (kN)	Strength reduction ($F_{u,test}$ / $F_{u,test,A}$)	Failure mode
1A	20	306.0	13.0	3.00	72.25	-	N
1B	200	303.0	13.0	3.00	73.77	1.02	N
1C	300	160.0	13.0	3.00	41.19	0.57	N
1D	400	123.0	13.0	3.00	30.63	0.42	N
2A	20	306.0	13.0	1.31	45.33	–	B
2B	200	303.0	13.0	1.31	43.34	0.96	B
2C	300	160.0	13.0	1.31	21.82	0.48	B
2D	400	123.0	13.0	1.31	19.00	0.42	B
3A	20	306.0	13.0	2.31	71.69	-	B+N
3B	200	303.0	13.0	2.31	71.76	1.00	B+N
3C	300	160.0	13.0	2.31	37.91	0.53	B+N
3D	400	123.0	13.0	2.31	30.08	0.42	B+N

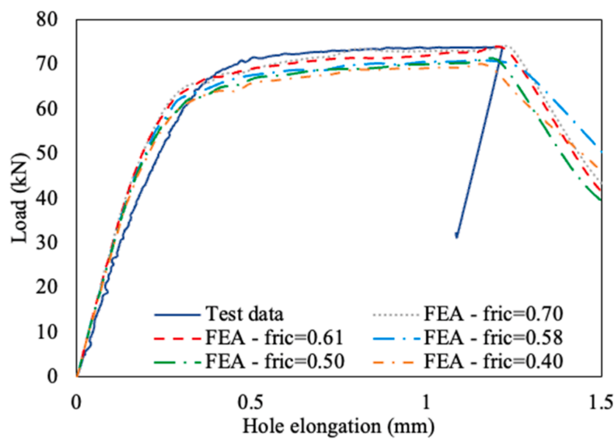

Fig. 11. Friction coefficient calibration process for specimen 1B.

3.2. Failure modes

Fig. 9 shows the observed failure modes for all specimens. Failure modes observed in the tests included net section failure, bearing failure, and mixed behaviour. All specimens in Group 1 failed by net section fracture (N), while those in Group 2 failed by bearing (B). Specimens in Group 3 exhibited mixed failure mode, with pronounced bearing deformations followed by a combined net-section fracture. This behaviour was intentionally achieved by specifying bolt spacings that caused net section and bearing failures to occur at comparable load levels. In particular, the specimens were designed using Eurocode-based calculations [22], with bolt spacings selected so that the predicted net-section and bearing resistances were comparable, with bearing being slightly lower.

In Group 1 specimens, net section failure consistently occurred at the inner bolt row. In tests C and D, where the aluminium plates were subjected to elevated temperatures, significant plastic deformation was observed before fracture, including noticeable narrowing of the plate width in the fracture region. For Group 2 specimens, which failed by bearing, failure typically initiated at the outer bolt hole. When the edge distance was smallest, material tearing occurred in front of the bolt, effectively splitting the plate. Under elevated temperatures (specimens C and D), the response was more ductile, leading to higher deformations around the holes. This led to a more pronounced bearing failure mode, as the plates could accommodate additional deformation even after reaching the peak load. Group 3 specimens exhibited a mixed failure mode, characterised by significant bearing deformation at the outer bolt, and net-section fracture at the inner bolt row. The extent of net-section fracture was influenced by material ductility, with preheated specimens (B and C) exhibiting sufficient ductility to accommodate bearing deformation until large deformations before fracture.

3.3. Load-displacement curves

The load-deformation curves obtained from the tests are reported in Fig. 10. The experimental resistances are summarised in Table 3, where $F_{u,test}$ represents the ultimate load recorded during testing. Table 3 also reports f_u and α_b which are codified variables defined in Section 5.1, as well as the strength reduction ratios compared to benchmark specimens ($F_{u,test,A}$). For the specimens A (no pre-heat), the ultimate load values ($F_{u,test}$) for specimens 1A and 3A were relatively consistent, ranging between 71–73 kN. It should be noted that for specimen 2A, data near the end of the test was lost, so the reported load–displacement curve only partially reflects the specimen's full response. Nevertheless, the testing machine data show a load plateau consistent with specimen 2B, supporting the reliability of the identified failure load. For specimens tested after being heated at 200 °C, the ultimate loads remained fairly consistent within each series, with only slight reductions (approximately 1–2 kN) compared to the results of the benchmark specimens. As the pre-test temperature increased to 300 °C and 400 °C, a more substantial reduction in ultimate strength was observed. This was accompanied by increased deformation and hole elongation. For instance, maximum recorded load for specimen Group 1 decreased progressively from 72.25 kN at 20 °C to 30.63 kN at 400 °C. The hole elongation at failure load

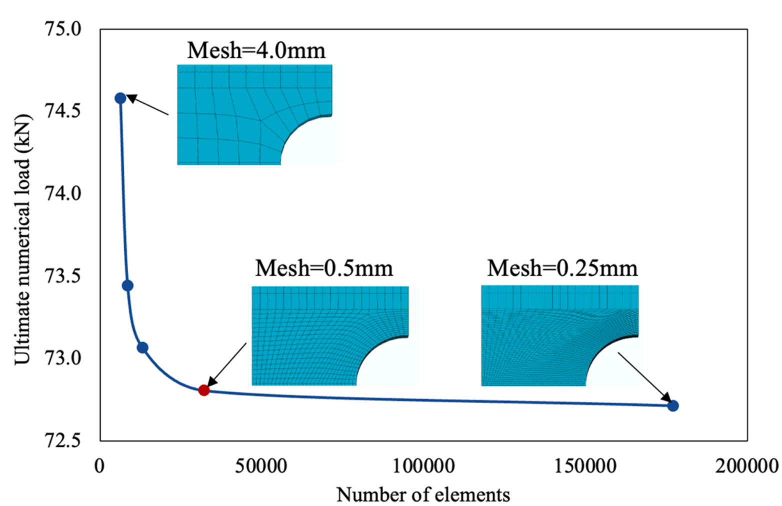

Fig. 12. Mesh sensitivity analysis.

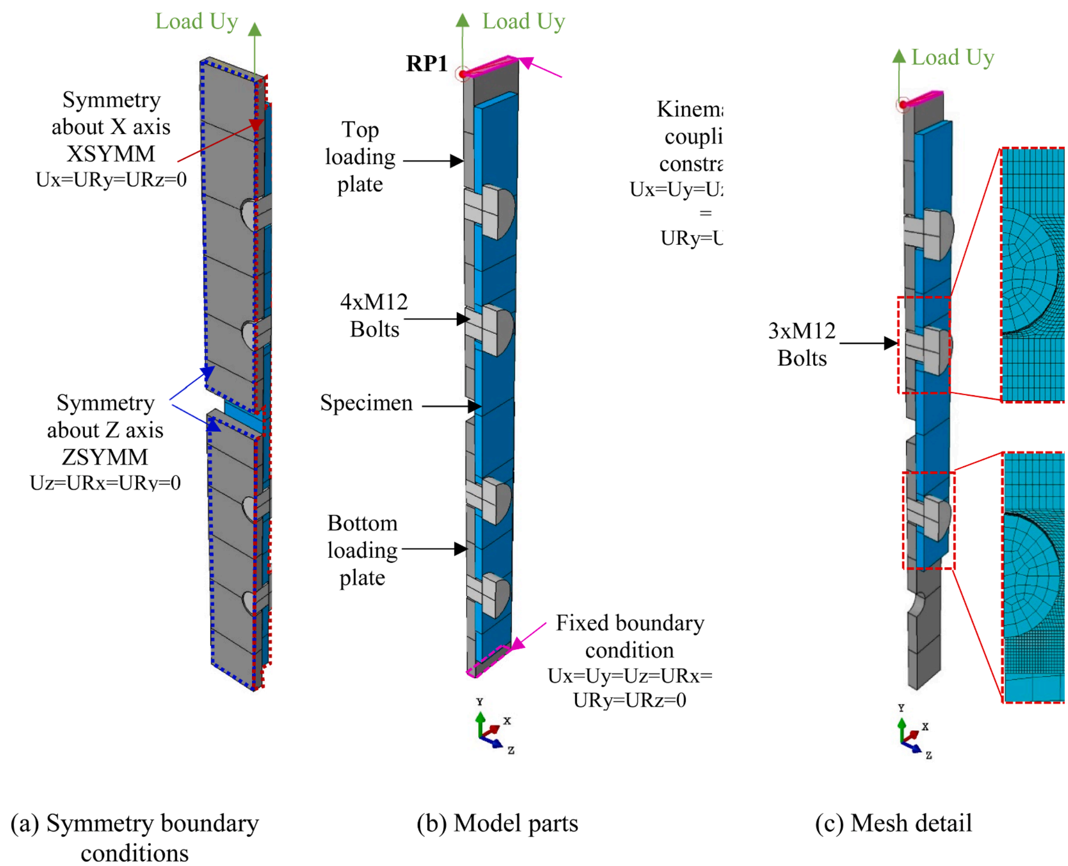

Fig. 13. Development of the FE models.

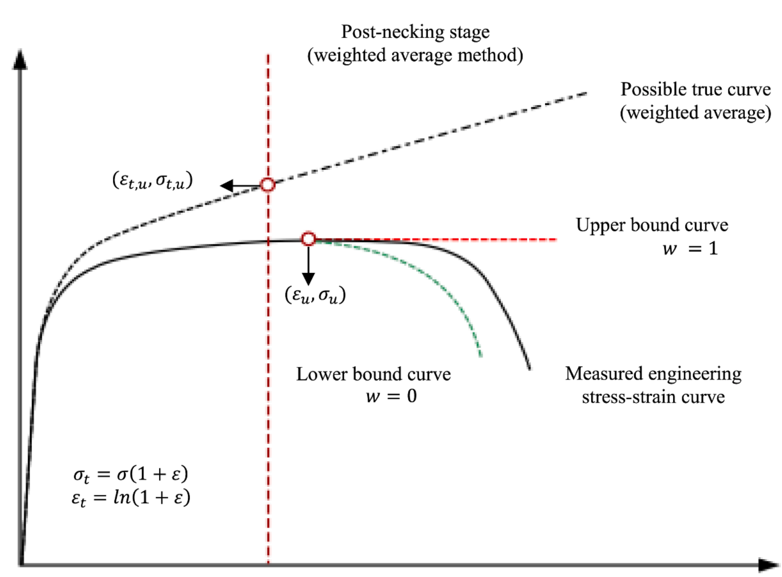

Fig. 14. Schematic representation of pre- and post-necking stress-strain response modelling using the weighted average method.

was under 2 mm for specimens 1A and 1B, but exceeded 2 mm and 3 mm for specimens 1C and 1D, respectively, indicating increased ductility with increasing pre-heating temperature. Similar trends were observed across all specimens. Overall, specimens tested after exposure to 300 °C (1C, 2C, 3C) experienced reductions in ultimate strength of approximately 30–50 % compared to those tested at 20 °C. The most substantial decreases were seen in the 400 °C specimens (1D, 2D, 3D), with strength reductions reaching 60 % in some cases.

4. Numerical modelling

The numerical modelling is introduced to extend the experimental dataset, enabling a broader and more robust assessment of existing design methods beyond the tested configurations. The general-purpose Finite Element (FE) software Abaqus [30] was used to develop numerical models of the double shear bolted connections to examine their response under static loading and varying geometric configurations.

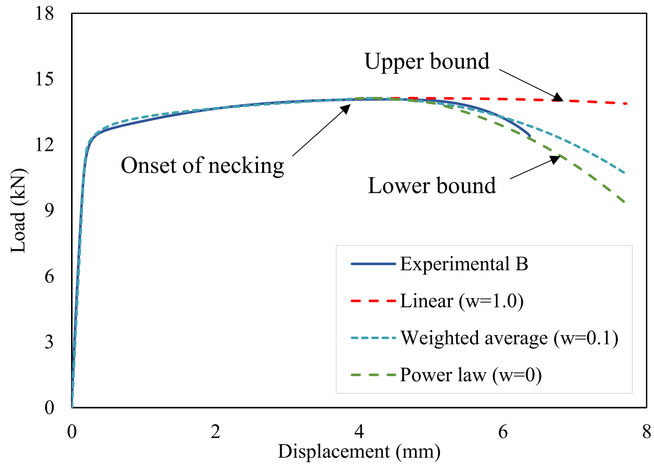

Fig. 15. Representative lower and upper bounds and calibration of weight factor w.

Table 4
Calibrated post-necking and fracture parameters.

Specimen	w	c_1	c_2
A	0.3	1.129	-3.925
B	0.1	1.129	-3.925
C	0.2	1.500	-2.525
D	0.0	1.500	-1.500

4.1. Modelling assumptions

Eight-node linear brick elements with reduced integration (C3D8R) were employed to discretise the geometry of all the model parts i.e., specimens, loading plates and bolts. To reduce computational cost, a quarter model of the connection was developed by exploiting symmetry in both the loading conditions and geometry. The bolt geometry was also simplified: the threaded region was represented as a smooth cylinder with an effective diameter corresponding to the bolt unthreaded area. The bolt head, nut, and shank were modelled as a single continuous piece, and their hexagonal profiles were approximated as cylinders. These simplifications are widely adopted in the literature and have been shown not to compromise the accuracy of the results [31,32]. No bolt preload was applied, given that in the tests the bolts were hand-tightened to obtain the snug-tight condition. Loading was applied as a prescribed displacement at the top loading plate in the y-axis direction. Contact interactions between all components were defined using the *"All with self"* * surface-to-surface contact approach in ABAQUS. A friction coefficient of 0.61, determined through a calibration process similar to [33], was applied via the *penalty* method for tangential behaviour, and *hard* contact was used for normal behaviour. The friction coefficient calibration process is shown in Fig. 11. Separation after contact was permitted. Kinematic coupling was applied to the top face of the loading plate, constraining all degrees of freedom and assigning RP1 as the controlling reference point. Full contact between the bolts and the loading plates was assumed at the start of the simulation, thus eliminating any initial bolt-hole clearance. Based on the sensitivity analysis, as shown in Fig. 12, a mesh size of 0.5 mm was employed in the anticipated fracture region to accurately capture the sharp stress variations, plastic strains, and the progression of fracture, while a coarser mesh was applied in other regions. This mesh configuration was found to provide accurate results without incurring excessive computational cost. Fig. 13 shows the boundary conditions, model components, and mesh for the 2 representative geometric configurations with one row of 4 bolts and 3 bolts.

A quasi-static explicit dynamic analysis was performed to enable fracture prediction without encountering convergence issues, while keeping computational time reasonable. Mass scaling was applied to increase the stable time increment, thereby reducing the total simulation time. To minimise inertial effects, the prescribed vertical displacement was applied using a smooth amplitude curve. The validity of this

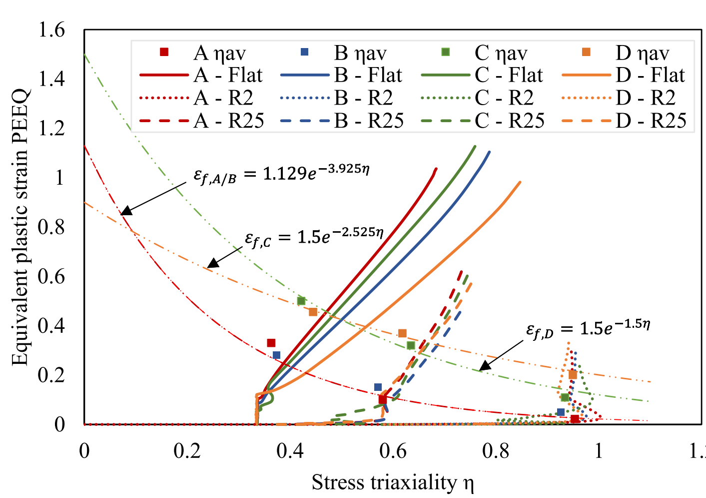

Fig. 16. Numerical evolution of stress triaxiality with plastic strain until fracture initiation and proposed equations.

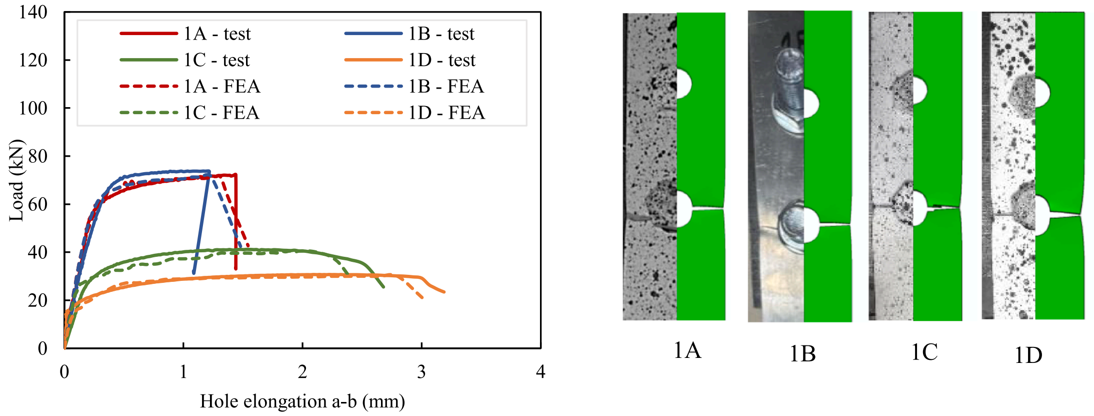

(a) Specimens Group 1

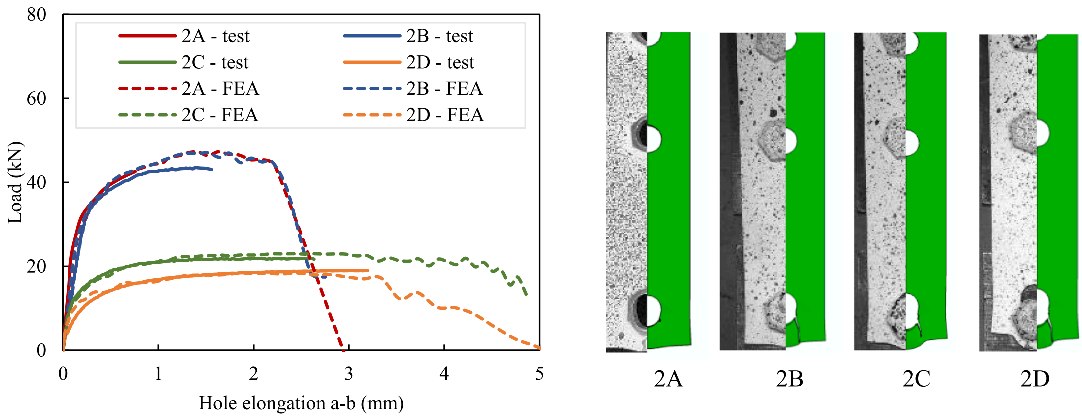

(b) Specimens Group 2

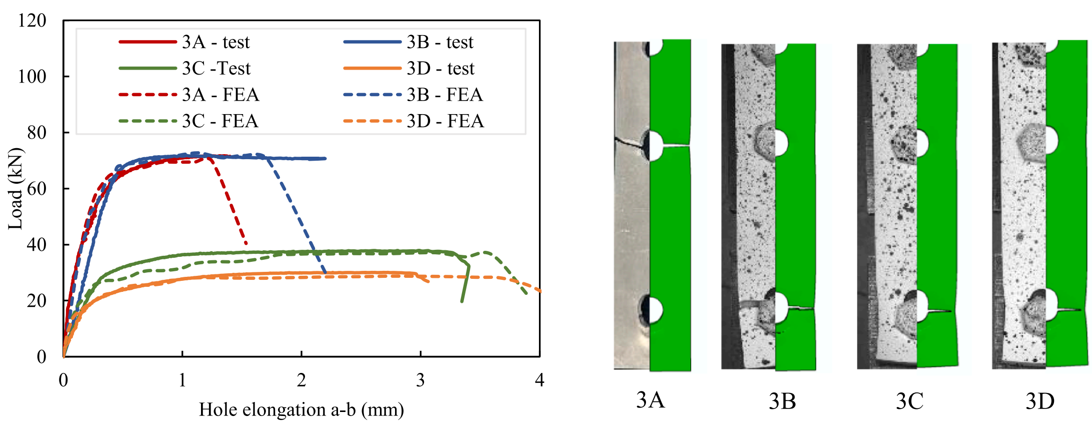

(c) Specimens Group 3

Fig. 17. Comparison of experimental and numerical load-deformation curves and failure modes.

approach was confirmed by monitoring the kinetic energy, which remained below 2 % of the internal energy throughout the analysis.

4.2. Material and fracture model

The pre-necking true stress–strain material response (σ_t-ε_t) was derived from the experimentally obtained engineering stress–strain data (σ-ε) (Fig. 3) to simulate the full-range plasticity of the aluminium alloy materials until the attainment of the ultimate tensile stress. The post-necking material response was modelled using the weighted average method [34]. This method assumes that the post-necking response can be approximated as a weighted average of a power-law and a linear extrapolation of the stress–strain curve beyond necking. These two curves represent the lower and upper bounds of the post-necking behaviour, respectively, as shown in Fig. 14. The approach is defined in Eqs. (1) and (2).

$$\varepsilon_t = \ln(1+\varepsilon) \tag{1}$$

$$\sigma_t = \left\{ \begin{array}{c} \sigma(1+\varepsilon) \text{ for } \varepsilon \leq \varepsilon_u \\ \sigma_{t,u}\left[\mathrm{w}(1+\varepsilon_t-\varepsilon_{t,u}) + (1-w)\left(\dfrac{\varepsilon_t}{\varepsilon_{t,u}}\right)^{\varepsilon_{t,u}} \right] \text{ for } \varepsilon > \varepsilon_u \end{array} \right\} \tag{2}$$

where ε_u, $\varepsilon_{t,u}$ and $\sigma_{t,u}$ are the engineering strain, true strain and true stress at the onset of necking (ultimate engineering tensile stress), and w

Table 5
Comparison of experimental and numerical loads.

Specimen	$F_{u,test}$ (kN)	$F_{u,FEA}$ (kN)	$F_{u,FEA}/F_{u,test}$	Mean	COV
1A	72.25	71.45	0.989	0.980	0.008
1B	73.77	71.38	0.968		
1C	41.19	40.53	0.984		
1D	30.63	30.02	0.980		
2A	45.33	47.29	1.043	1.038	0.041
2B	43.34	47.02	1.085		
2C	21.82	23.01	1.054		
2D	19.00	18.41	0.969		
3A	71.69	69.67	0.972	0.979	0.021
3B	71.76	72.66	1.012		
3C	37.91	37.04	0.977		
3D	30.08	28.74	0.955		
		Mean (All)	1.00		
		COV (All)	0.04		

Table 6
List of key parameters included in the parametric study.

Set	Temperature (°C)	e_1 (mm)	e_2 (mm)	Number of models
A	20	10.4, 13.0, 15.6, 26.0, 32.5, 39.0	15.6, 20.0, 26.0, 52.0	24
		20.8, 45.5, 52.0	52.0	3
B	200	10.4, 13.0, 15.6, 26.0, 32.5, 39.0	15.6, 52.0	12
C	300	10.4, 13.0, 15.6, 26.0, 32.5, 39.0	15.6, 52.0	12
D	400	10.4, 13.0, 15.6, 26.0, 32.5, 39.0	15.6, 52.0	12
			Total models:	63

is a weighting factor controlling the shape of the true stress-strain curve in the post-necking range, with $0 \leq w \leq 1$, determined through an iterative trial and error approach until the numerical load-displacement material response is in close agreement with the experimental load-displacement curves. This process was carried out independently for each temperature level, with Fig. 15 showing an illustrative example for the fitting procedure of flat coupon B (200 °C). The optimal values w for benchmark (A) and pre-heated material (B, C and D for material pre-heated at 200 °C, 300 °C and 400 °C respectively) are reported in Table 4.

The fracture model was developed based on the procedure reported in [27] assuming that the strain at fracture is a function of the stress triaxiality. Fig. 16 illustrates the relationship between the stress triaxiality at the centre of the specimen, where fracture begins, and the equivalent plastic strain (PEEQ) for all the tested coupons. Stress triaxiality was monitored numerically at the integration point located at the centre of each specimen and recorded as a function of equivalent plastic strain during loading. The average stress triaxiality was obtained by computing the area under the triaxiality–plastic strain curve and dividing it by the total accumulated equivalent plastic strain. The strain at fracture, $\varepsilon_{f,}$ is defined in Eqs. (3), where η_{av} represents the average triaxiality, ε is the equivalent plastic strain [35].

$$\eta_{av} = \frac{1}{\varepsilon_f}\int_0^{\varepsilon_f}\eta(\varepsilon)d\varepsilon \tag{3}$$

$$\varepsilon_f = \ c_1 e^{c_2\eta} \tag{4}$$

The relationships between the plastic fracture strain ε_f and stress triaxiality η is assumed exponential as defined by Eq. (4), where c_1 and c_2 are material dependent parameters, calibrated as the best match for the numerical values. The adopted values for c_1 and c_2, determined through an iterative trial and error approach until the numerical material response is in close agreement with the experimental load-displacement curves, are summarised in Table 4 and Fig. 16. Similar process has been successfully applied in [27]. These curves were used as a fracture initiation criterion using the ductile damage material option in ABAQUS and specifying a very low (virtually zero) energy for the fracture propagation.

4.3. Validation of the FE models

The FE model incorporating fracture was validated by comparing the numerically predicted load–displacement responses and failure modes with corresponding experimental results, as illustrated in Fig. 17, and summarised in Table 5. Overall, the numerical predictions show good agreement with the experimental data, and the fracture behaviour is accurately captured. The average ratio of numerical to experimental ultimate load for Group 1 specimens 1 is 0.980, for Group 2 specimens is 1.038, and for Group 3 specimens is 0.979, with a coefficient of variation of 0.008, 0.041, and 0.021, respectively. The close match between experimental and numerical curves for all specimens confirms the effectiveness of the adopted fracture modelling approach in predicting failure for the 6082-T6 lap joints for the four studied temperatures. It is worth noting that in some cases the experimental curves did not capture the fracture, i.e., the descending branch of the load–displacement curve, due to failure occurring at the back plate or DIC accuracy being lost. Nevertheless, these samples are still validated based on their ultimate load.

4.4. Parametric study

Having validated the numerical model, parametric studies were performed. Since in earlier design rules [27] both the end and edge distances were assumed to be affecting the bearing resistance, both e_1 and e_2 were varied for each of the 4 pre-heating temperatures considered in the tests. The values of bolt spacing, bolt diameter $d = 12.0$mm, and clearance hole $d_0 = 13.0$mm used in the tests remained unchanged. The effect of plate thickness t was not investigated, as previous studies have shown that variations in t result only in proportional changes in ultimate resistance and have minimal impact on connection behaviour. All models employ the material model (including fracture) for 6082-T6 previously discussed, while the bolts were assumed to be elastic for all models to simplify modelling, since bolt fracture is beyond the scope of this study and was not observed in the tests. While the assumption of elastic bolt behaviour is appropriate for the scope of this study, explicit modelling of bolt plasticity may be required in cases involving large deformations, where bolt yielding and redistribution of forces can potentially influence failure mode predictions. The investigated parameters of the 63 models are summarised in Table 6. The results of the parametric study are summarised in Table 7, where the numerically obtained failure modes are also reported.

The total number of samples failing by bearing (B) is 39, while 24 failed by net section fracture (N). Fig. 18 shows the tensile and shear stress distributions at the ultimate load for representative connections failing by bearing and net section fracture. The tensile and shear stresses along the identified failure paths at mid-thickness of the plates are plotted [36]. For the B specimen in Fig. 18 (a), the highest stress along the net tensile plane occurs at the edge of the bolt hole and decreases with increasing distance toward the plate edge. This stress gradient results in compressive stresses caused by rotation of the section as bearing failure develops. Similarly, the shear stresses along the effective shear plane are highest near the bolt hole edge, where failure initiates. In contrast, as expected, the N specimen in Fig. 18 (b) shows no compressive stress in the net section, and the shear stresses are generally smaller than those in the B specimen.

Six reference points (a, b, c, d, e, and f) were defined on the FE plate, as illustrated in Fig. 19, where p_1 is the distance between the centre of the bolt holes. The total deformation of the connection is typically quantified as the extension of the plate along the loading direction,

Table 7
Numerical parametric study results.

No	T (°C)	e_1 (mm)	e_1/d_0	e_2 (mm)	e_2/d_0	b (mm)	h (mm)	f_u (MPa)	$F_{u,\ FEA}$	Failure Mode $_{FEA}$
1	20	10.4	0.8	15.6	1.20	31.2	180.4	306	26.6	N
2	20	13.0	1.0	15.6	1.20	31.2	183.0	306	35.5	N
3	20	15.6	1.2	15.6	1.20	31.2	185.6	306	42.7	N
4	20	26.0	2.0	15.6	1.20	31.2	196.0	306	50.2	N
5	20	32.5	2.5	15.6	1.20	31.2	202.5	306	50.1	N
6	20	39.0	3.0	15.6	1.20	31.2	209.0	306	50.4	N
7	20	10.4	0.8	20.0	1.54	40.0	180.4	306	21.2	B
8	20	13.0	1.0	20.0	1.54	40.0	183.0	306	35.2	B
9	20	15.6	1.2	20.0	1.54	40.0	185.6	306	44.2	B
10	20	26.0	2.0	20.0	1.54	40.0	196.0	306	69.2	N
11	20	32.5	2.5	20.0	1.54	40.0	202.5	306	73.1	N
12	20	39.0	3.0	20.0	1.54	40.0	209.0	306	73.0	N
13	20	10.4	0.8	26.0	2.00	52.0	180.4	306	22.6	B
14	20	13.0	1.0	26.0	2.00	52.0	183.0	306	33.9	B
15	20	15.6	1.2	26.0	2.00	52.0	185.6	306	42.2	B
16	20	26.0	2.0	26.0	2.00	52.0	196.0	306	73.2	N
17	20	32.5	2.5	26.0	2.00	52.0	202.5	306	85.4	N
18	20	39.0	3.0	26.0	2.00	52.0	209.0	306	93.6	N+C
19	20	10.4	0.8	52.0	4.00	104.0	180.4	306	25.1	B
20	20	13.0	1.0	52.0	4.00	104.0	183.0	306	34.4	B
21	20	15.6	1.2	52.0	4.00	104.0	185.6	306	42.8	B
22	20	20.8	1.6	52.0	4.00	104.0	190.8	306	61.1	B
23	20	26.0	2.0	52.0	4.00	104.0	196.0	306	74.3	B
24	20	32.5	2.5	52.0	4.00	104.0	202.5	306	85.6	B
25	20	39.0	3.0	52.0	4.00	104.0	209.0	306	89.7	B
26	20	45.5	2.5	52.0	4.00	104.0	215.5	306	98.4	B
27	20	52.0	3.0	52.0	4.00	104.0	222.0	306	100.0	B
28	200	10.4	0.8	15.6	1.20	31.2	180.4	303	26.3	B
29	200	13.0	1.0	15.6	1.20	31.2	183.0	303	34.8	N
30	200	15.6	1.2	15.6	1.20	31.2	185.6	303	42.6	N
31	200	26.0	2.0	15.6	1.20	31.2	196.0	303	50.1	N
32	200	32.5	2.5	15.6	1.20	31.2	202.5	303	50.1	N
33	200	39.0	3.0	15.6	1.20	31.2	209.0	303	50.5	N
34	200	10.4	0.8	52.0	4.00	104.0	180.4	303	25.7	B
35	200	13.0	1.0	52.0	4.00	104.0	183.0	303	34.0	B
36	200	15.6	1.2	52.0	4.00	104.0	185.6	303	43.0	B
37	200	26.0	2.0	52.0	4.00	104.0	196.0	303	73.8	B
38	200	32.5	2.5	52.0	4.00	104.0	202.5	303	85.0	B
39	200	39.0	3.0	52.0	4.00	104.0	209.0	303	93.1	B
40	300	10.4	0.8	15.6	1.20	31.2	180.4	160	12.7	B
41	300	13.0	1.0	15.6	1.20	31.2	183.0	160	17.8	B
42	300	15.6	1.2	15.6	1.20	31.2	185.6	160	21.3	B
43	300	26.0	2.0	15.6	1.20	31.2	196.0	160	26.1	N
44	300	32.5	2.5	15.6	1.20	31.2	202.5	160	26.4	N
45	300	39.0	3.0	15.6	1.20	31.2	209.0	160	26.6	N
46	300	10.4	0.8	52.0	4.00	104.0	180.4	160	12.8	B
47	300	13.0	1.0	52.0	4.00	104.0	183.0	160	17.5	B
48	300	15.6	1.2	52.0	4.00	104.0	185.6	160	22.2	B
49	300	26.0	2.0	52.0	4.00	104.0	196.0	160	36.0	B
50	300	32.5	2.5	52.0	4.00	104.0	202.5	160	43.3	B
51	300	39.0	3.0	52.0	4.00	104.0	209.0	160	48.4	B
52	400	10.4	0.8	15.6	1.20	31.2	180.4	123	11.0	B
53	400	13.0	1.0	15.6	1.20	31.2	183.0	123	14.4	B
54	400	15.6	1.2	15.6	1.20	31.2	185.6	123	17.5	N
55	400	26.0	2.0	15.6	1.20	31.2	196.0	123	20.0	N
56	400	32.5	2.5	15.6	1.20	31.2	202.5	123	19.9	N
57	400	39.0	3.0	15.6	1.20	31.2	209.0	123	20.2	N
58	400	10.4	0.8	52.0	4.00	104.0	180.4	123	10.9	B
59	400	13.0	1.0	52.0	4.00	104.0	183.0	123	14.2	B
60	400	15.6	1.2	52.0	4.00	104.0	185.6	123	17.4	B
61	400	26.0	2.0	52.0	4.00	104.0	196.0	123	28.5	B
62	400	32.5	2.5	52.0	4.00	104.0	202.5	123	33.3	B
63	400	39.0	3.0	52.0	4.00	104.0	209.0	123	35.7	B

measured between points a and b [37]. This elongation results from four main factors: bolt protrusion (c to d), bolt hole bearing or embedding (b to c), elongation of the gross section (a to f), and elongation of the net section (e to f). Fig. 20 presents the deformation patterns of two representative specimens, B and N. In Fig. 20 (a), where bolt protrusion dominates the deformation, the connection fails primarily by bearing, commonly associated with small end distances e_1. In contrast, Fig. 20 (b) shows that in specimens with relatively small edge distances (e_2) and large end distances (e_1), deformation is mainly attributed to net section elongation, leading to failure by net section fracture.

Finally, it is noteworthy that in model 18, out-of-plane plate deformations in front of the bolt, commonly known as curling, was observed, as shown in Fig. 21. This deformation corresponds to a form of local buckling of the plate under compressive stresses [38]. Since curling

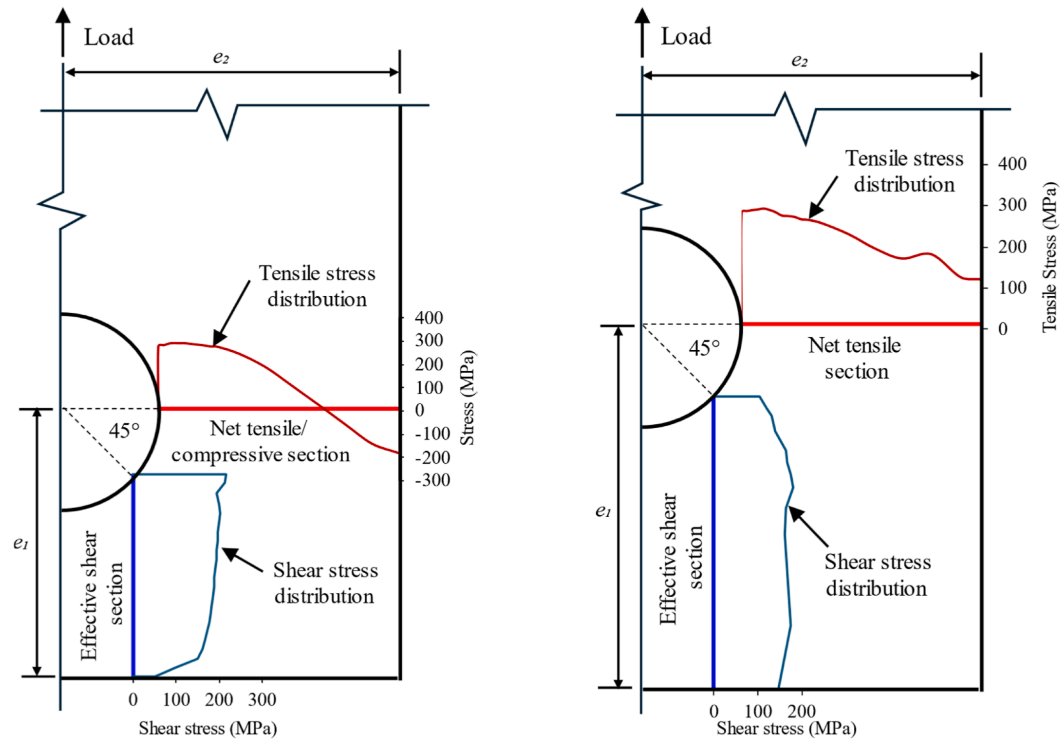

(a) Model No. 15 B (e_1/d_0=1.2, e_2/d_0=2.0) (b) Model No. 17 N (e_1/d_0=2.5, e_2/d_0=2.0)

Fig. 18. Ultimate tensile and shear stress distributions across net tensile and effective shear sections for representative models (plotted on undeformed configuration).

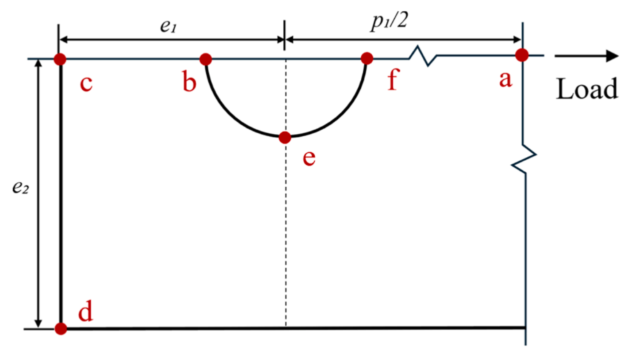

Fig. 19. Reference points assigned to plates in the FE models.

is a known behaviour in bolted connections with thin steel plates and, in this case, occurred concurrently with failure mode N, it was not considered further in the discussion.

5. Assessment of current design standards and design recommendations

This section assesses the applicability of existing design standards in predicting bearing and net-section fracture failures of aluminium alloy connections. The evaluation of bearing failure predictions, based on design provisions from several codes, is carried out using 39 FEA simulations ("B" in Table 7) and 8 experimental data points ("B" in Table 3). These assessments have also led to a new design proposal, explained in Section 5.2. Cases in which net-section failure ("N") governed—typically observed in joints with large end distances (e_1) and small edge distances (e_2)—have been used for the evaluation of the European design provisions. This assessment was based on 24 FEA simulations ("N" in Table 7) and 4 experimental data points ("N" in Table 3). All partial safety factors are set to unity.

5.1. Design predictions

The design provisions outlined in this section will be used for the assessment presented in Section 5.3.

5.1.1. Bearing resistance - EN 1999-1-1 (2023) [22]

According to [22], the resistance $(F_{b,Rd})$ to bearing failure is given by Eq. (5)

$$F_{b,Rd} = \frac{\alpha_b f_u d t}{\gamma_{M2}} \tag{5}$$

Where f_u the characteristic ultimate strength of the aluminium plate material, d the bolt diameter, t the thickness of the plate and γ_{M2} the partial safety. The bearing resistance factor α_b for end bolts can be evaluated from Eq. (6)

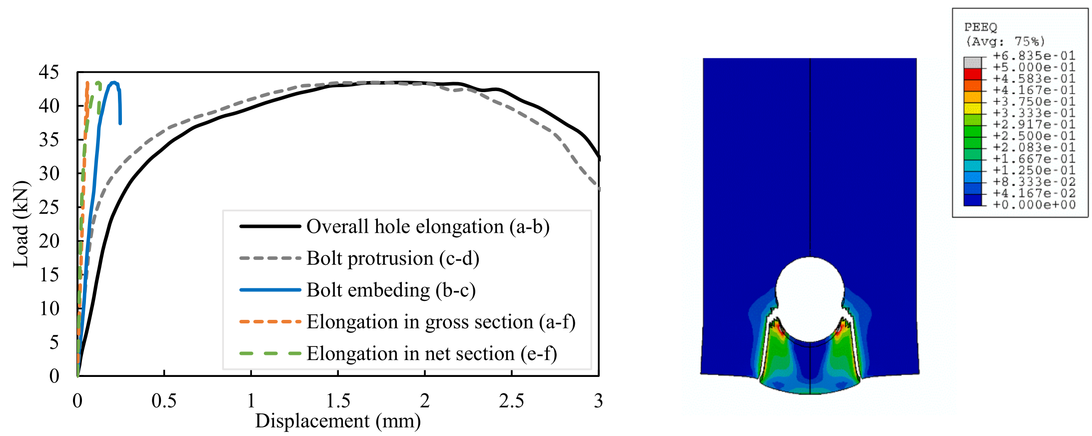

(a) Model No. 9 B (e_1/d_0=1.2, e_2/d_0=1.5)

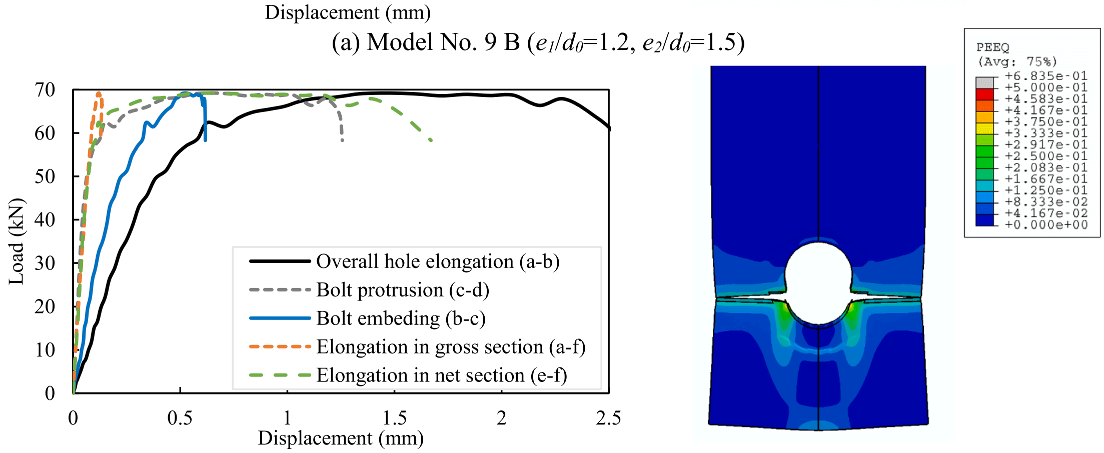

(b) Model No. 10 N (e_1/d_0=2.0, e_2/d_0=1.5)

Fig. 20. Components of deformation for representative connection samples.

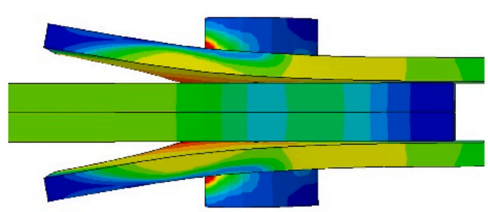

Fig. 21. Deformed shape of connection susceptible to curling (model 18).

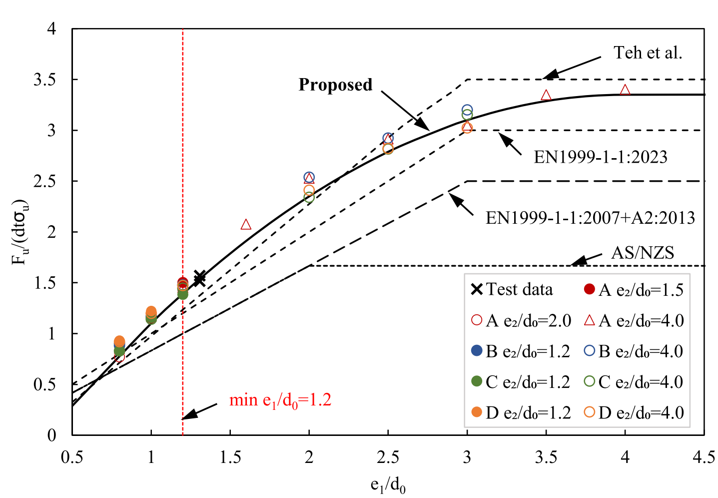

Fig. 22. Effect of end distance e_1 on the bearing resistances of double shear lap-joint connections and comparison with design provisions.

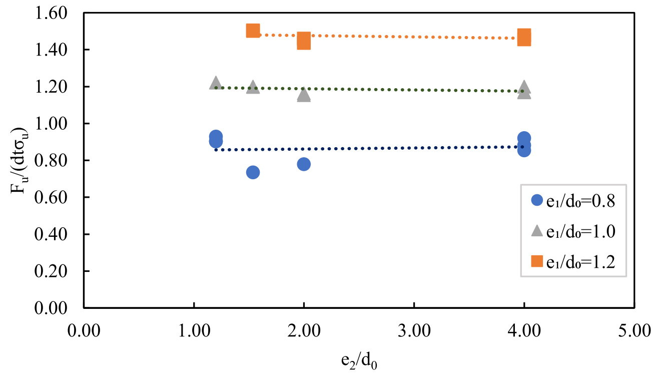

Fig. 23. Effect of end distance e_2 on the bearing resistances of double shear lap-joint connections and comparison with design predictions.

Table 8
Assessment of bearing resistance design predictions.

FEA/Exp Data			*EN 1999-1-1 (2023)* [22]	*EN 1999-1-1 (2007+A2-2013)* [39]	*Teh and Uz* [40,43]	*AS/NZS 1664.1:1997* [41]		
No	T (°C)	$F_{u,\,FEA\ or\ Exp}$	$F_{u,B,\,EC9,\,2023}$ / $F_{u,FEA\ or\ Exp}$	$F_{u,B,\,EC9,\,2013}$ / $F_{u,FEA\ or\ Exp}$	$F_{u,B,\,Teh\ and\ Uz}$ / $F_{u,FEA\ or\ Exp}$	$F_{u,AS/NSZ}$ / $F_{u,FEA\ or\ Exp}$	a_{prop}	$F_{u,B,\,proposed}$ / $F_{u,FEA\ or\ Exp}$
2A	20	45.33	0.85	0.71	0.89	1.08	1.54	1.00
2B	200	43.34	0.88	0.73	0.92	1.12	1.54	1.03
2C	300	21.82	0.92	0.77	0.97	1.17	1.54	1.08
2D	400	19.00	0.81	0.68	0.85	1.04	1.54	0.96
3A	20	71.69	0.83	0.79	1.10	0.68	2.63	1.08
3B	200	71.76	0.82	0.78	1.08	0.68	2.63	1.07
3C	300	37.91	0.82	0.78	1.08	0.68	2.63	1.07
3D	400	30.08	0.79	0.75	1.05	0.65	2.63	1.03
7	20	21.2	0.89	0.75	0.80	0.75	0.79	0.88
8	20	35.2	0.83	0.70	0.81	0.70	1.10	0.92
9	20	44.2	0.80	0.66	0.82	0.66	1.39	0.92
13	20	22.6	1.04	0.87	0.93	0.87	0.79	1.03
14	20	33.9	0.87	0.72	0.84	0.72	1.10	0.95
15	20	42.2	0.84	0.70	0.86	0.70	1.39	0.97
19	20	25.1	0.94	0.78	0.84	0.78	0.79	0.92
20	20	34.4	0.85	0.71	0.83	0.71	1.10	0.94
21	20	42.8	0.82	0.69	0.85	0.69	1.39	0.95
22	20	61.1	0.77	0.64	0.84	0.64	1.91	0.92
23	20	74.3	0.79	0.66	0.90	0.66	2.35	0.93
24	20	85.6	0.86	0.71	1.00	0.57	2.79	0.96
25	20	89.7	0.98	0.82	1.15	0.55	3.10	1.02
26	20	98.4	0.90	0.75	1.04	0.50	3.29	0.98
27	20	100.0	0.88	0.73	1.03	0.49	3.35	0.98
28	200	26.3	0.89	0.49	0.79	0.738	0.79	0.87
34	200	25.7	0.91	0.76	0.81	0.76	0.79	0.90
35	200	34.0	0.86	0.71	0.83	0.71	1.10	0.94
36	200	43.0	0.81	0.68	0.84	0.68	1.39	0.94
37	200	73.8	0.79	0.66	0.90	0.66	2.35	0.93
38	200	85.0	0.86	0.71	1.00	0.57	2.79	0.95
39	200	93.1	0.94	0.78	1.09	0.52	3.10	0.97
40	300	12.7	0.97	0.54	0.86	0.81	0.79	0.96
41	300	17.8	0.86	0.48	0.84	0.72	1.10	0.95
42	300	21.3	0.87	0.48	0.89	0.72	1.39	1.00
46	300	12.8	0.96	0.46	0.861	0.802	0.79	0.95
47	300	17.5	0.86	0.44	0.854	0.730	1.10	0.96
48	300	22.2	0.83	0.69	0.85	0.69	1.39	0.96
49	300	36.0	0.84	0.70	0.96	0.70	2.35	0.99
50	300	43.3	0.85	0.74	1.04	0.59	2.79	0.99
51	300	48.4	0.95	0.79	1.11	0.53	3.10	0.98
52	400	11.0	0.86	0.48	0.77	0.72	0.79	0.85
53	400	14.4	0.82	0.45	0.80	0.68	1.10	0.90
58	400	10.9	0.87	0.72	0.78	0.72	0.79	0.86
59	400	14.2	0.83	0.69	0.81	0.69	1.10	0.92
60	400	17.4	0.81	0.68	0.84	0.68	1.39	0.94
61	400	28.5	0.83	0.69	0.94	0.69	2.35	0.97
62	400	33.3	0.89	0.74	1.04	0.59	2.79	0.99
63	400	35.7	0.99	0.83	1.16	0.55	3.10	1.03
		Mean (all)	**0.87**	**0.70**	**0.92**	**0.71**		**0.96**
		COV (all)	**0.07**	**0.14**	**0.12**	**0.21**		**0.06**

$$\alpha_b = min\left(\frac{e_1}{d_0};\frac{3f_{ub}}{f_u};3\right) \tag{6}$$

Where f_{ub} is the characteristic ultimate strength of the bolt material. Note that Eqs. (5)-(6) are based on the most recent version of the Eurocode.

5.1.2. Bearing resistance - EN 1999-1-1 (2007+A2-2013) [39]

In the previous version of Eurocode 9 (EN 1999-1-1:2007+A2:2013), the bearing resistance was defined by Eqs. (7)–(9), whilst, Eqs. (5)–(6) presented previously, represent the updated formulations. A significant change is that in the most recent version of EN 1999-1-1 the edge distance e_2 is not assumed to influence the bearing resistance.

$$F_{b,Rd} = \frac{k_1\alpha_b f_u dt}{\gamma_{M2}} \tag{7}$$

Where the bearing resistance factor depends on factors α_b and k_1 accounting for bolt spacing parallel and perpendicular to the applied load respectively, as defined by Eqs. (8)-(9).

$$\alpha_b = min\left(a_d;\frac{f_{ub}}{f_u};1\right) \text{ where } a_d = \frac{e_1}{3d_o} \text{ for end bolts and } a_d = \frac{p_1}{3d_o} - \frac{1}{4} \text{ for inner bolts} \tag{8}$$

$$k_1 = \min\left(2.8\frac{e_2}{d_o} - 1.7;\ 2.5\right) \text{ for edge bolts and } k_1 = \min\left(1.4\frac{p_2}{d_o} - 1.7;\ 2.5\right) \text{ for inner bolts} \tag{9}$$

5.1.3. Bearing resistance - Teh and Uz [40,43]

Based on experimental findings, Teh and Uz [40,43] proposed the design model given in Eq. (10) for predicting bearing failure. This equation defines the bearing resistance of a bolted connection based on material (f_u) and geometric parameters (e_1, d_0, t, d) as defined earlier. The expression takes the minimum of two values: a geometry-dependent term, which accounts for the adverse effect of small end distance e_1 and an upper limit, representing a maximum bearing capacity.

$$F_{B,Teh\ and\ Uz} = \min\left[1.2(e_1 - 0.25d_0)tf_u;\ 3.5dtf_u\right] \tag{10}$$

5.1.4. Bearing resistance - AS/NZS 1664.1:1997 [41]

These equations define the bearing capacity of a bolted connection as a function of plate geometry and material properties. Eq. (11) gives the nominal bearing capacity, while Eq. (12) adjusts the stress factor f_B based on the end distance e_1, where when $e_1 \geq 2d$, full bearing capacity is allowed. When $e_1 < 2d$, a linear reduction is applied to account for the reduced effectiveness of the bearing area.

$$F_{AS/NZS} = 2dtf_B \tag{11}$$

$$f_B = \begin{cases} \min\left(f_{0.2};\frac{f_u}{1.2}\right) & \text{for } e_1 \geq 2d \\ \frac{e_1}{2d}\min\left(f_{0.2};\frac{f_u}{1.2}\right) & \text{for } e_1 < 2d \end{cases} \tag{12}$$

5.1.5. Net section fracture – EN 1999-1-1 [22,39]

The resistance of the net section fracture is given by Eq. (13), where $A_{net}$is the net section area, with deduction for holes and f_u the characteristic ultimate strength of the aluminium plate material. The same equation is proposed in both version of EN 1999-1-1 (2007+A2-2013) [39] and EN 1999-1-1 (2023) [22].

$$F_{net,Rd} = 0.9A_{net}f_u/\gamma_{M2} \tag{13}$$

5.2. Proposed design equation

In this section, the experimentally and numerically obtained data are used to assess the applicability of the bearing resistance factor α_b given by EN 1999-1-1 (2007+A2-2013) [39], by EN 1999-1-1 (2023) [22], and the alternative model proposed by Teh and Uz [40,43]. To perform this assessment while considering the effects of end and edge distances, e_1 and e_2 respectively, the numerically obtained ultimate load corresponding to bearing failure F_u, divided by two, was normalised by the bearing coefficient β, calculated as the product of bolt diameter d, thickness t and ultimate tensile stress of the plate f_u, and plotted against the normalised bolt end distance e_1/d_0 for each value of e_2/d_0 in Fig. 22. In this figure, the codified design provisions [22,39,41] and Teh and Uz proposal [40,43] are also plotted for different values of e_1/d_0. From assessing EN 1999-1-1 [22], it is noted that the design standard does not allow for $e_1/d_0 \leq 1.2$, however the relevant design curves were extrapolated below this limit to allow the assessment of the suitability of the design rules for lap joints with smaller e_1/d_0 values. The FE data presented in Fig. 22, contrary to the available linear models [22,39,41] follow a curved trend, emphasising therefore the need for a more accurate equation for α_b. The proposed new model for α_b, derived from calibrating an elliptical function equation, is presented in Eq. (14). This formulation expresses a_b as a function of e_1/d_0, and is calibrated against the experimental and numerical findings, thereby enhancing the accuracy of the predictions. Similar approaches have been adopted by [42] and [43].

$$\alpha_b = min\left[3.35; 3.35 - 0.25\left(4 - \frac{e_1}{d_0}\right)^2\right] \tag{14}$$

To more accurately assess the potential effect of e_2/d_0 on the bearing resistance, the data points for all temperatures have been grouped and plotted against their value for small values of e_1/d_0, as shown in Fig. 23. It is clear that the effect of e_2/d_0 on the bearing resistance is minimal,

Table 9
Assessment of net section fracture eurocode design predictions.

FEA/Exp Data			EN 1999-1-1 (2023) [22]
No	T (°C)	$F_{u,\ FEA\ or\ Exp}$	$F_{u_{net},\ EC9}$ / $F_{u,FEA\ or\ Exp}$
1A	20	72.25	0.82
1B	200	73.33	0.80
1C	300	41.19	0.76
1D	400	30.63	0.78
1	20	26.57	0.88
2	20	35.49	0.83
3	20	42.71	0.83
4	20	50.16	0.80
5	20	50.05	0.80
6	20	50.38	0.80
10	20	69.22	0.85
11	20	73.07	0.81
12	20	72.99	0.82
16	20	73.17	0.80
17	20	85.41	0.86
18	20	93.58	0.92
29	200	34.8	0.84
30	200	42.6	0.82
31	200	50.1	0.79
32	200	50.1	0.79
33	200	50.5	0.79
43	300	35.2	0.80
44	300	37.5	0.79
45	300	37.3	0.79
54	400	17.5	0.81
55	400	20.0	0.81
56	400	19.9	0.81
57	400	20.2	0.80
54	400	17.5	0.81
		Mean (all)	**0.81**
		COV (all)	**0.04**

Table 10
Effect of temperature on the design accuracy – based on experimental and numerical average values [COV].

	EN 1999-1-1 (2023) [22] - Bearing	EN 1999-1-1 (2007+A2-2013) [39] - Bearing	Teh and Uz [40,43] - Bearing	AS/NZS 1664.1:1997 [41] - Bearing	Design Proposal - Bearing	EN 1999-1-1[22,39] – Net Section Fracture	Average
A (room)	0.87 [0.08]	0.73 [0.08]	0.91 [0.12]	0.69 [0.20]	0.96 [0.05]	0.83 [0.03]	0.83 [0.13]
B (200C)	0.86 [0.06]	0.70 [0.13]	0.92 [0.12]	0.72 [0.24]	0.96 [0.06]	0.81 [0.03]	0.83 [0.13]
C (300C)	0.82 [0.18]	0.62 [0.23]	0.87 [0.24]	0.68 [0.29]	0.92 [0.20]	0.79 [0.23]	0.78 [0.14]
D (400C)	0.85 [0.07]	0.67 [0.18]	0.90 [0.15]	0.70 [0.19]	0.95 [0.08]	0.80 [0.02]	0.81 [0.13]

with small variations caused by data variation. This justifies excluding the effect of e_2/d_0 from the latest version of EN 1999-1-1 [22].

5.3. Assessment of design standards

A comparison of FEA and experimental data with design values from various design codes [22,39,41] and proposed models found in the literature [40,43] is presented in Table 8 and Table 9. With regards to the bearing resistance design prediction, the updated EN 1999-1-1 (2023) [22] shows improved accuracy compared to the previous EN 1999-1-1 (2007+A2-2013) [39], with a higher mean of predicted-to-FE/experimental ratio of 0.87 (compared to 0.70) and a lower coefficient of variation, indicating better consistency and alignment with the test data. The AS/NZS design code considerably underpredicts the strength, with a mean ratio of 0.71, and high variability. The Teh and Uz [40,43] model demonstrates improved accuracy, with a mean ratio of 0.92. However, the design method using the proposed Eq. (14) demonstrates the best agreement with the FEA/experimental data, achieving a mean ratio of 0.96 and maintaining a low coefficient of variation (COV) of 0.06, supporting its potential as a more accurate and reliable design approach.

Table 10 presents the design ratio for prediction for the various assessed temperature levels, indicating generally conservative design predictions. At room temperature (Condition A), all models show relatively comparable accuracy, with average values around 0.83. As temperature increases to 200 °C and 300 °C (Conditions B and C), a general reduction in accuracy is observed for most codified methods, particularly for EN 1999-1-1 (2007+A2:2013) and AS/NZS 1664.1:1997, which consistently underestimate capacity. In contrast, the proposed design approach maintains a high level of accuracy across all temperature levels, demonstrating greater robustness under thermal degradation. Generally, it appears that the design equations calibrated for room temperature remain applicable at elevated temperatures. No clear trend is observed in design accuracy with increasing temperature, which can be attributed to the incorporation of temperature-dependent material properties in the FE analyses.

6. Conclusions and future work

The experimental testing and numerical modelling of 6082-T6 aluminium lap connections after exposure to high temperatures, considering four temperature levels, have provided valuable insights into the material behaviour and structural performance. The investigation was limited to 6082-T6 aluminium alloy subjected to a prescribed heating and cooling protocol.

Material testing was carried out on eight flat coupons of 6082-T6 aluminium alloy. The results showed that the ratio of proof strength at 300 °C and 400 °C was 0.34 and 0.16, respectively, when compared to room-temperature values. In addition, twelve tests on aluminium lap joints were conducted, covering three geometries and four temperature levels. The observed failure modes included net-section fracture, bearing failure, and combinations of the two. Flat grooved coupon tests were performed at the same four temperature levels. Using these data, a calibrated material model for aluminium alloys was developed, incorporating post-necking behaviour and fracture through a weighted-average approach. A triaxiality-dependent fracture criterion was also applied, enabling accurate finite element simulation of full-range plastic deformation and the onset of fracture.

Following the successful development and validation of the finite element model, a comprehensive parametric study consisting of sixty-three analyses was completed, and all output data were reported. Of the total FE specimens, 39 failed by bearing and 24 by net-section fracture. Specimens that failed in bearing exhibited higher tensile and shear stresses near the bolt holes, indicating compressive stresses caused by section rotation, whereas specimens failing by net-section fracture showed lower shear stresses and no compressive stress in the net section.

Normalising the ultimate load with the bearing coefficient and plotting it against the ratio e_1/d_0 enabled the development of a new equation for the bearing resistance factor α_b, which demonstrated better agreement with the experimental data than existing code-based expressions. An assessment of bearing-failure strength prediction showed that current design codes are generally conservative. The proposed design method exhibited the closest agreement with the finite-element and experimental results, with a mean ratio $F_{u,B,proposed}/F_{u,FEA\ or\ Exp} = 0.96$ and a coefficient of variation of 0.06, outperforming codified procedures in both accuracy and consistency. The proposed bearing factor was calibrated using 39 FE simulations and 8 experimental results and is applicable only to configurations with $e_1/d_0 = 0.8$–4.0, $e_2/d_0 = 1.2$–4.0, a bolt diameter of 12 mm, and temperatures between 200 °C and 400 °C; extrapolation beyond these ranges requires further validation.

Similarly, an evaluation of strength predictions for net-section fracture according to Eurocode provisions resulted in a conservative design outcome, with $F_{u,\mathrm{net,\ EC9}}/F_{u,FEA\ or\ Exp}=0.81$ and a coefficient of variation of 0.04, indicating the need for further research in this area. Overall, design ratios remain generally conservative across all temperature ranges, and no clear trend in accuracy was observed with increasing temperature, although the proposed approach consistently outperformed codified methods in terms of strength prediction.

Future research should extend the proposed equation to other aluminium alloys, joint configurations, and loading conditions to improve general applicability. Particular attention should be given to the influence of bolt spacing p_1 on bearing failure occurring between bolts and the role of post-fire ductility on the bearing resistance. As the experimental programme was limited to a specific lap-joint geometry under monotonic loading, further experimental and numerical studies are recommended to validate failure mechanisms and residual strength across a wider range of temperatures, materials, loading conditions, and connection geometries for a broader range of aluminium joint configurations under post-fire conditions.

CRediT authorship contribution statement

Michaela Gkantou: Writing – original draft, Investigation, Conceptualization. **Manuela Cabrera:** Writing – original draft, Investigation. **Marina Bock:** Writing – review & editing, Conceptualization. **Marios Theofanous:** Writing – review & editing, Conceptualization.

Declaration of competing interest

The authors declare that they have no known competing financial interests or personal relationships that could have appeared to influence the work reported in this paper.

Acknowledgements

The authors would like to thank the School of Engineering and Built Environment of Liverpool John Moores University for their financial support. They would also like acknowledge the support received from Mr. Richard Clarke, technician at the School of Engineering and Built Environment, Liverpool John Moores University, for his assistance with the experimental work. The computations described in this paper were performed using the University of Birmingham's BlueBEAR HPC service, which provides a High Performance Computing service to the University's research community. See http://www.birmingham.ac.uk/bear for more details.

Data availability

Data will be made available on request.

References

[1] E. Georgantzia, M. Gkantou, G.S. Kamaris, Aluminium alloys as structural material: a review of research, Eng. Struct. 227 (2021), https://doi.org/10.1016/j.engstruct.2020.111372.

[2] S. Bin Ali, G.S. Kamaris, M. Gkantou, K.D. Kansara, Concrete-filled and bare 6082-T6 aluminium alloy tubes under in-plane bending: experiments, finite element analysis and design recommendations, Thin-Walled Struct. 172 (2022) 108907, https://doi.org/10.1016/j.tws.2022.108907. Mar.

[3] S. Bin Ali, G.S. Kamaris, M. Gkantou, Flexural buckling behaviour of concrete-filled double skin aluminium alloy columns, Eng. Struct. 275 (2023) 115316, https://doi.org/10.1016/j.engstruct.2022.115316. Jan.

[4] Z. Wang, Y. Wang, B. Li, Y. Zhang, Experimental and numerical study on seismic behaviour of aluminium alloy frames, J. Build. Eng. 50 (2022) 104231, https://doi.org/10.1016/j.jobe.2022.104231. Jun.

[5] Y. Sun, The use of aluminum alloys in structures: review and outlook, Structures 57 (2023) 105290, https://doi.org/10.1016/j.istruc.2023.105290. Nov.

[6] A. Pisapia, E. Nastri, V. Piluso, A. Formisano, F. Massimo Mazzolani, Experimental campaign on structural aluminium alloys under monotonic and cyclic loading, Eng. Struct. 282 (2023) 115836, https://doi.org/10.1016/j.engstruct.2023.115836. May.

[7] K. Jiang, S. Li, T. Guo, Y. Liang, O. Zhao, Net section fracture of aluminium alloy angle-to-plate connections: Testing, modelling and design, Eng. Struct. 326 (2025) 119450, https://doi.org/10.1016/j.engstruct.2024.119450. Mar.

[8] B. Li, et al., Mechanical characteristic and stress-strain modelling of friction stir welded 6061-T6 aluminium alloy butt joints, Thin-Walled Struct. 198 (2024) 111645, https://doi.org/10.1016/j.tws.2024.111645. May.

[9] M.-N. Su, B. Young, Material properties of normal and high strength aluminium alloys at elevated temperatures, Thin-Walled Struct. 137 (2019) 463–471, https://doi.org/10.1016/j.tws.2019.01.012. Apr.

[10] D. Skejić, I. Ćurković, M.J. Rukavina, Behaviour of aluminium structures in fire, a review, Appl. Struct. Fire Eng. (2016), https://doi.org/10.14311/asfe.2015.047. Jan.

[11] Y. Sun, W. Cheng, K. Chen, Experimental study of in-fire and post-fire material response of high-strength aluminium alloys, J. Build. Eng. 91 (2024) 109581, https://doi.org/10.1016/j.jobe.2024.109581. Aug.

[12] Y. Sun, K. Zhang, G. Gong, Material properties of structural aluminium alloys after exposure to fire, Structures 55 (2023) 2105–2111, https://doi.org/10.1016/j.istruc.2023.07.027. Sep.

[13] Y. Sun, G. Han, Post-fire capacity of aluminium alloy rectangular hollow sections under compression, Eng. Struct. 327 (2025) 119602, https://doi.org/10.1016/j.engstruct.2024.119602. Mar.

[14] Z. Wang, et al., Structural fire behaviour of aluminium alloy structures: review and outlook, Eng. Struct. 268 (2022) 114746, https://doi.org/10.1016/j.engstruct.2022.114746. Oct.

[15] Z. Wang, J. Li, Y. Ouyang, O. Zhao, Post-fire material behaviour, residual properties and predictive models of recycled 6061-T6 aluminium alloys, Constr. Build. Mater. 484 (2025) 141805, https://doi.org/10.1016/j.conbuildmat.2025.141805. Jul.

[16] Z. Wang, J. Li, Y. Ouyang, O. Zhao, Post-fire local buckling of recycled 6061-T6 aluminium alloy SHS stub columns, Eng. Struct. 343 (2025) 120972, https://doi.org/10.1016/j.engstruct.2025.120972. Nov.

[17] J. Maljaars, G. De Matteis, Structural response of aluminium T-Stub connections at elevated temperatures and fire, Key Eng. Mater. 710 (2016) 127–136, https://doi.org/10.4028/www.scientific.net/KEM.710.127. Sep.

[18] H. Liu, X. Liu, Z. Chen, Y. Ouyang, J. Yin, Mechanical properties of bolted connections for aluminum alloy structures at elevated temperatures, Thin-Walled Struct. 157 (2020) 107067, https://doi.org/10.1016/j.tws.2020.107067. Dec.

[19] Z. Wang, C. Ma, X. Yun, Q. Han, B. Li, Z. Wang, Experimental study on structural performance of 7A04-T6 high-strength aluminium alloy shear connections in and after fire, Eng. Struct. 309 (2024) 118028, https://doi.org/10.1016/j.engstruct.2024.118028. Jun.

[20] X. Guo, S. Zhu, X. Liu, K. Wang, Study on out-of-plane flexural behavior of aluminum alloy gusset joints at elevated temperatures, Thin-Walled Struct. 123 (2018) 452–466, https://doi.org/10.1016/j.tws.2017.11.045. Feb.

[21] X. Guo, X. Duan, J. Liu, S. Chen, Study on flexural behavior of aluminum alloy portal frame beam-column joint at high temperature, Thin-Walled Struct. 215 (2025) 113477, https://doi.org/10.1016/j.tws.2025.113477. Oct.

[22] EN 1999-1-1, Eurocode 9: Design of aluminium structures — Part 1-1: General structural rules. Brussels: CEN, CEN. European Committee for Standardisation, 2023.

[23] Y. Sun, Z. Fu, Y. Song, J. Xia, Cross-Sectional Behavior of Aluminum Alloy Channel Section Stub Columns after Exposure to Fire, J. Struct. Eng. 149 (7) (2023), https://doi.org/10.1061/JSENDH.STENG-12383. Jul.

[24] Simmal, "Simmal Ltd. Aluminium extrusions & stockholding preston," https://simmal.com/.

[25] BS EN ISO 6892-1, "Metallic materials. Tensile testing. Method of test at room temperature," 2019.

[26] W.M. Quach, J.G. Teng, K.F. Chung, Three-stage full-range stress-strain model for stainless steels, J. Struct. Eng. 134 (9) (2008) 1518–1527, https://doi.org/10.1061/(ASCE)0733-9445(2008)134:9(1518). Sep.

[27] M. Cabrera, M. Theofanous, M. Bock, Behaviour and design of bolted aluminium flange cleats, Thin-Walled Struct. 215 (2025) 113447, https://doi.org/10.1016/j.tws.2025.113447. Oct.

[28] Y. Bai, X. Teng, T. Wierzbicki, On the application of stress triaxiality formula for plane strain fracture testing, J. Eng. Mater. Technol. 131 (2) (2009), https://doi.org/10.1115/1.3078390. Apr.
[29] E.L. Salih, L. Gardner, D.A. Nethercot, Bearing failure in stainless steel bolted connections, Eng. Struct. 33 (2) (2011) 549–562, https://doi.org/10.1016/j.engstruct.2010.11.013. Feb.
[30] S. I. Karlsson Hibbitt, "ABAQUS/Standard user's manual volumes I-III and ABAQUS CAE manual," 2016.
[31] O. Yapici, M. Theofanous, S. Afshan, H. Yuan, S. Dirar, Numerical modelling of stainless steel bolted T-stubs in tension, Thin-Walled Struct. 177 (2022) 109432, https://doi.org/10.1016/j.tws.2022.109432. Aug.
[32] M. Cabrera, W. Tizani, J. Ninic, Fusion of experimental and numerical data for development of Extended Hollo-bolt component based model, Eng. Struct. 321 (2024) 118932, https://doi.org/10.1016/j.engstruct.2024.118932. Dec.
[33] M. Bock, S. Gupta, M.F. Hassanein, Y. Sheng, A Slenderness-based method for web crippling design of aluminum tubular sections, J. Struct. Eng. 148 (12) (2022), https://doi.org/10.1061/JSENDH.STENG-11796. Dec.
[34] Y. Ling, Uniaxial true stress-strain after necking, AMP J. Technol. 5 (1996) 47–48.
[35] Y. Bao, T. Wierzbicki, On fracture locus in the equivalent strain and stress triaxiality space, Int. J. Mech. Sci 46 (1) (2004) 81–98, https://doi.org/10.1016/j.ijmecsci.2004.02.006. Jan.
[36] Y. Song, X.-M. Lin, M.C.H. Yam, K. Ke, Block shear failure of austenitic stainless steel bolted connections, Thin-Walled Struct. 193 (2023) 111251, https://doi.org/10.1016/j.tws.2023.111251. Dec.
[37] E.L. Salih, L. Gardner, D.A. Nethercot, Bearing failure in stainless steel bolted connections, Eng. Struct 33 (2) (2011) 549–562, https://doi.org/10.1016/j.engstruct.2010.11.013. Feb.
[38] T.S. Kim, H. Kuwamura, T.J. Cho, A parametric study on ultimate strength of single shear bolted connections with curling, Thin-Walled Struct. 46 (1) (2008) 38–53, https://doi.org/10.1016/j.tws.2007.08.009. Jan.
[39] EN 1999-1-1, Eurocode 9: Design of aluminium structures — Part 1-1: General structural rules. (2007+A2-2013) Brussels: CEN, European Committee for Standardisation, 2013.
[40] L.H. Teh, M.E. Uz, Ultimate shear-out capacities of structural-steel bolted connections, J. Struct. Eng. 141 (6) (2015), https://doi.org/10.1061/(ASCE)ST.1943-541X.0001105. Jun.
[41] AS/NZS 1664.1:1997, "Standards Australia, aluminium structures part 1: limit state design," Sydney, Australia, 1997.
[42] Y. Song, X.-M. Lin, M.C.H. Yam, Y. Zhang, K. Ke, J. Wang, Bearing and tearout of austenitic and duplex stainless steel bolted connections, Thin-Walled Struct. 205 (2024) 112585, https://doi.org/10.1016/j.tws.2024.112585. Dec.
[43] L.H. Teh, M.E. Uz, Combined bearing and shear-out capacity of structural steel bolted connections, J. Struct. Eng. 142 (11) (2016), https://doi.org/10.1061/(ASCE)ST.1943-541X.0001573. Nov.